Journal of Power Sources 253 (2014) 55–63

Contents lists available at ScienceDirect

Journal of Power Sources

journal homepage: www.elsevier.com/locate/jpowsour

Preparation of three-dimensional hybrid nanostructure-encapsulated sulfur cathode for high-rate lithium sulfur batteries

Jing Xie, Juan Yang, Xiangyang Zhou*, Youlan Zou, Jingjing Tang, Songcan Wang, Feng Chen

School of Metallurgy and Environment, Central South University, Changsha 410083, China

HIGHLIGHTS

- A novel approach for high-rate lithium sulfur batteries.
- A three-dimensional hybrid structure by incorporating the merits of MWCNTs and graphene.
- The RGO@NWCNTs-W/S composite cathode exhibits an admirable high-rate performance.
- This work makes much sense to the structure designing of novel sulfur-based materials.

GRAPHICAL ABSTRACT

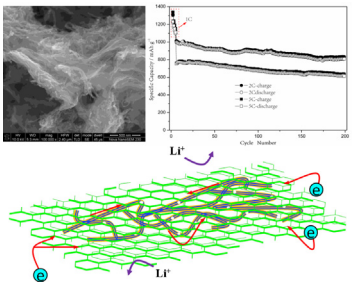

ARTICLE INFO

Article history:
Received 29 August 2013
Received in revised form
11 December 2013
Accepted 16 December 2013
Available online 22 December 2013

Keywords:
Sulfur composite
Multi-walled carbon nanotube webs
Graphene coating
Hybrid nanostructure
Lithium-sulfur batteries

ABSTRACT

A three-dimensional hybrid nanostructure incorporating the merits of the MWCNTs webs (MWCNTs-W) and the reduced graphene oxide (RGO) is designed to improve the high-rate cycling performance of the lithium-sulfur batteries. Owing to the excellent Li^+ ion and electronic transport properties of the MWCNTs-W and the RGO, this unique structure can provide a three-dimensional conductive network and promote rapid charge-transfer reaction at the cathode. Furthermore, because of the rough surface and porous structure of the MWCNTs after activation with KOH, and the special adsorption ability of the RGO, the soluble polysulfide intermediates can be effectively trapped in the cathode. Therefore, when evaluating the electrochemical properties of the RGO@MWCNTs-W/S composite as the cathode material for lithium-sulfur batteries, it exhibits an excellent cyclical stability and high rate performance. In particular, even at an ultrahigh rate (5 C), a discharge capacity as high as 620 mAh g^{-1} is still retained for the RGO@MWCNTs-W/S composite with 68.93 wt% sulfur after 200 cycles, and the average coulombic efficiency is 96%.

1. Introduction

As the key electrical energy storage devices for portable electronics and power tools, rechargeable lithium ion batteries have achieved great development during the past decades [1,2]. However, the commercialized lithium ion batteries will become insufficient for the future electric vehicles due to the low capacity of conventional cathode materials (for example, ~150 mAh g^{-1} for layered oxides and ~170 mAh g^{-1} for $LiFePO_4$) [3,4]. Developing novel electrode materials with higher gravimetric and volumetric capacities is becoming increasingly urgent. Sulfur, as one of the most abundant elements on the earth, can react with metallic lithium to form Li_2S by a two-electron reaction, and offers a high theoretical capacity of 1675 mAh g^{-1} and a high theoretical energy density of 2600 Wh kg^{-1}, making it a potential high capacity cathode material for the next rechargeable batteries [5].

* Corresponding author. Tel./fax: +86 073188836329.
E-mail address: hncsyjy308@163.com (X. Zhou).

0378-7753/$ – see front matter © 2013 Elsevier B.V. All rights reserved.
http://dx.doi.org/10.1016/j.jpowsour.2013.12.074

However, due to some major problems, commercial applications of lithium sulfur batteries have not been very successful even after several decades of research. Such major problems include the insulating nature of sulfur (5×10^{-30} S cm^{-1} at 25 °C) and its reduced products, leading to low utilization of active material [6]. In addition, the high solubility of polysulfide intermediates in the electrolyte and the shuttle of the high-order polysulfides (Li_2S_x, $2 < x \leq 8$) between the electrodes during cycling both result in loss of active material and low coulombic efficiency [5]. Moreover, sulfur cathodes undergo significant volume expansion and contraction during charge and discharge. This volume change (~80% for sulfur) can result in pulverization of the initial particle morphology and cause the loss of electrical contact between active materials and the cathode framework [4,7].

In recent years, various strategies including the optimization of the organic electrolyte or additives [8–12], the application of protective films for the lithium anode [13,14], the fabrication of sulfur/conductive polymer composites [15–18] and sulfur/carbon composites [2–4,6,7,19–33], were developed to improve the electrochemical performance of sulfur cathodes. Among the strategies, encapsulating sulfur in the porous carbon materials (such as order mesoporous and microporous carbon [2,4,19–24], carbon nanotubes [25–31], porous fibers [4,7,29,32] et al.), which can minimize or avoid the shuttle of polysulfides because of their large surface area, high porous structure and strong adsorption ability, has been demonstrate to be one of the most highly desired methods to improving the cycle life of lithium-sulfur batteries.

While, owing to the inevitable dissolution of the polysulfides into the electrolyte through the channels of the porous carbon, especially at high rates, achieving a high capacity and cycling performance for sulfur/carbon cathode under high-rate conditions remains a challenge [21]. It is noted that the multi-walled carbon nanotubes (MWCNTs) are an attractive choice as the carbon matrix and electric conductor for high-rate sulfur cathodes due to their excellent electrical and unique structure. Because of their high aspect ratio, MWCNTs can provide faster Li^+ diffusion pathways, which will contribute to improve the rate performance of the sulfur cathode [26,28,30]. However, on account of the low surface areas and limited pore volumes, amount of sulfur would be crystallized on the outer surface of the MWCNTs, which would easily dissolve into the electrolyte and lead to the capacity fading. However, if the closed ends of the MWCNTs were opened and much more pores on the walls were created, the sulfur would be incorporated into the channels of the MWCNTs and the diffusion of polysulfides would be further minimized. Fortunately, the above assumption has been achieved by activation of the MWCNTs with KOH [33–35]. Moreover, according to the recent studies and our previous work, forming hybrid structure with highly conductive carbons material, such as PEG/mesoporous carbon hybrid nanostructure [2], graphene@CMK-3 hybrid nanostructure [36], PEG/graphene hybrid nanostructure [37], graphene/CNTs hybrid nanostructure [38] and PPy/PEG-modified CNTs hybrid nanostructure [39], is another promising method to further improve the electrochemical performance of the sulfur cathodes. In this work, we developed a three-dimensional hybrid nanostructure by incorporating the merits of the MWCNTs and the RGO to improve the high-rate cycling performance of the lithium-sulfur batteries (Fig. 1 shows the schematic diagram of the steps for synthesizing the hybrid nanostructure). First, activation of MWCNTs with KOH at high temperature was employed to obtain porous MWCNTs and achieve a MWCNTs webs structure (MWCNTs-W). Next, sulfur was incorporated into MWCNTs-W via a simple melt-diffusion method. Then the MWCNTs-W/S composites were pre-modified by the cationic surfactant (SDS) to carry up positive charge. Finally, the GO nanosheets with abundant negatively charged surface functional groups were conducted to self-assemble on the surface of the MWCNTs-W/S composites by electrostatic attraction [40]. In addition to the excellent adsorption ability of RGO and MWCNTs-W in trapping soluble polysulfides intermediates, both of them can also provide fast Li^+ diffusion pathways [25–30,36,37,41–44]. What's more, the unique three-dimensional hybrid nanostructure can form an effective three-dimensional electronically conductive network due to the excellent conductivity of RGO and MWCNTs-W. As a result, the RGO@MWCNTs-W/S with a three-dimensional hybrid

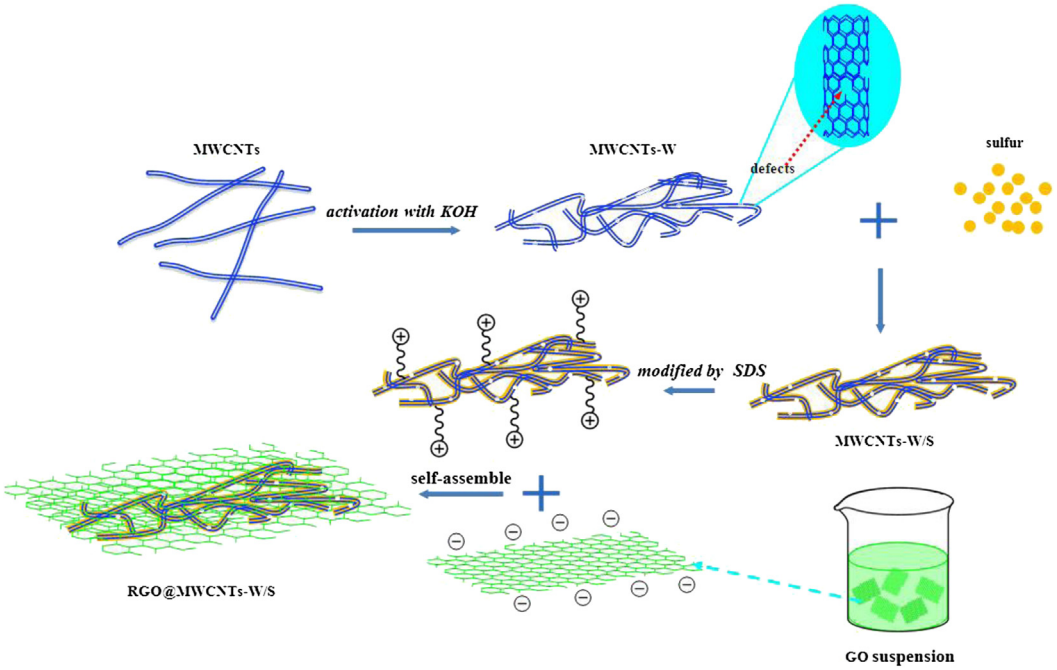

Fig. 1. The schematic diagram of the steps for synthesizing the RGO@MWCNTs-W/S composite.

nanostructure achieved an admirable high-rate capability and cycling performance.

2. Experimental

2.1. Preparation of the composite

MWCNTs treatment 1.5 g MWCNTs (purity of >95%, diameters of 10–20 nm, XF Nano, Co. Ltd, China) were physically mixed with KOH powder at the KOH/MWCNTs mass ratio of 7:1 in 20 ml alcohol–water solution ($v/v = 1{:}1$). After drying at 110 °C for 12 h, the activation process was carried out at 800 °C for 1 h at a heating rate of 5 °C min^{-1} under N_2 flow (300 ml min^{-1}). Finally, the sample was washed with 1.0 mol L^{-1} HCl for 2 h and filtered until there was no Cl^- detected by 1.0 mol L^{-1} $AgNO_3$. The activated MWCNTs-W was obtained after drying at 100 °C in an oven for 24 h.

MWCNTs-W/S preparation The MWCNTs-W/S composite was prepared via a simple melt-diffusion method. The activated MWCNTs-W was ground together with sulfur to achieve ~80 wt% of sulfur in the resultant MWCNTs-W/S composite, and then maintained in a sealed Teflon container for 12 h at 155 °C, followed by another 2 h at 250 °C under argon condition. The prepared MWCNTs-W/S composite was dispersed in 200 mL aqueous solution in which 5 ml of 1 wt% SDS (Sodium Dodecyl Sulfate) aqueous solution was added, and the mixture was sonicated for 30 min to achieve a black homogeneous aqueous suspension.

RGO@MWCNTs-W/S preparation Graphene oxide (GO) was synthesized by oxidation of graphite using improved Hummers' method as reported elsewhere [45]. A certain amount of GO aqueous suspension (10.0 mg mL^{-1}) was diluted to 1.0 mg mL^{-1} with distilled water. The dispersed MWCNTs-W/S aqueous solution was then added into the GO aqueous suspension drop by drop with string. The solution was allowed to stir for 2 h, a certain amount of hydrazine hydrate ($N_2H_4 \cdot H_2O$) was subsequently added to reduce graphene oxide to graphene. After stirring for 12 h at room temperature, the RGO@MWCNTs-W/S composite was collected by consecutive centrifugation and water-washing cycles as well as legalization.

2.2. Characterization of materials

Characterization of the as-prepared samples were carried out by scanning electron microscopy (SEM, JSM-6360LV, Japan), transmission electron microscopy (TEM, JEM-2100F, Japan), X-ray diffraction (XRD, Rigaku-TTRIII, Japan), Fourier transform infrared spectroscopy (FTIR, Nicolet 6700) and Raman spectroscopy (Lab-RAM Hr800). The content of sulfur in the MWCNTs-W/S composite and the RGO@MWCNTs-W/S composite were calculated based on the thermogravimetric analysis (TGA, SDTQ600) data.

2.3. Electrochemical test

The RGO@MWCNTs-W/S composite cathode slurry was prepared by mixing the as-prepared RGO@MWCNT-W/S composite (80 wt%), polyvinylidene fluoride (PVDF) binder (10 wt%) and conductive carbon black (10 wt%) with *N*-methyl-2-pyrrolidinone (NMP). The slurries were coated on an aluminum foil and dried in a vacuum oven at 60 °C for 24 h. The electrodes were cut into disks of 10 mm in diameter. The cell assembly was carried out in an argon-filled glove box (Super 1220/750, Shanghai Mikrouna Co. Ltd.) in which H_2O concentration was kept below 1ppm (An associated XDT-PM-PB dewpoint transmitter and GPR-1900 ppm oxygen analyzer can monitor the working condition of the glove box.). Lithium metal ($\Phi = 1.54$ cm) was used as the counter electrode, and a polyethylene film was used as the separator. The electrolyte was 1.0 M $LiN(CF_3SO_2)_2$ (LiTFSI) and 0.1 M $LiNO_3$ in a mixed solvent of dimethoxyethane (DME) and 1,3-dioxolane (DOL) at a volume ratio of 1:1, which was purchased from Zhangjiagang Guotai-Huarong New Chemical Materials Co., Ltd (Jiangsu, China). The cells were cycled in the potential range of 1.7–2.8 V versus Li/Li^+. In this study, 1 C corresponds to a current density value of 1680 mA g^{-1}-sulfur, the specific capacity was corrected based on the mass of sulfur, and a typical sulfur mass loading on the electrode was 0.8–0.9 mg cm^{-2}. Electrochemical impedance spectroscopy (EIS) measurements were performed with an impedance analyzer in the 100 kHz to 10 mHz frequency range in automatic sweep mode from high to low frequency. Cyclic voltammograms (CV) experiment was performed in the range of 1.6–3.0 V at a scanning rate 0.2 mV s^{-1}.

3. Results and discussion

In order to further verify the defects on the MWCNTs after activation with KOH, FTIR and Raman measurements were carried out. From the Raman results as shown in Fig. 2 (a), two obvious peaks at ~1350 cm^{-1}, which is assigned to the D bands corresponding to the disordered graphite, and ~1570 cm^{-1}, which is assigned to the G bands corresponding to a splitting of the E_{2g} stretching mode of graphite can be observed [33]. The intensity ratio of D/G bands (I_D/I_G) can be used to evaluate the extent of the modification or defect on the MWCNTs [33,35]. The I_D/I_G ratio of the MWCNTs decreases from 1.07 to 0.95 after the activation process, which implies more defects exist on the activated MWCNTs-W. The types of the chemical groups on the surface of the MWCNTs were characterized by FTIR and the corresponding results are shown in Fig. 2 (b). It can be clearly seen that a conspicuous band at ~1063 cm^{-1} appears in the FTIR spectra of the activated MWCNTs-W, which can be assigned to the C–O stretching vibration [33,46]. Compared to the raw MWCNTs, more oxygen-containing function groups on the surface of the activated MWCNTs-W could enhance

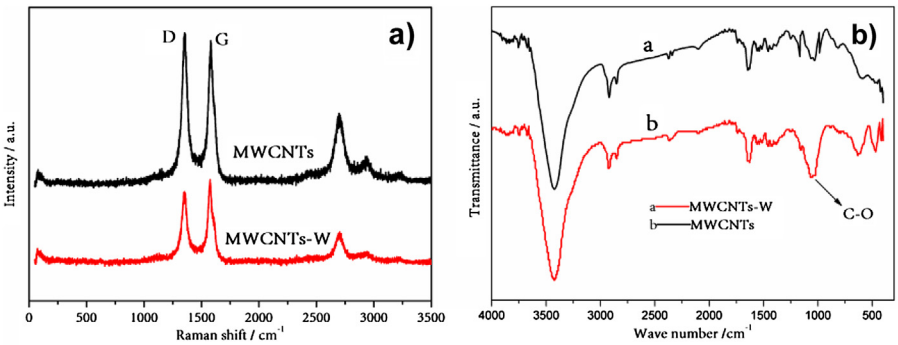

Fig. 2. (a) the Raman and (b) the FTIR spectra of the raw MWCNTs and the activated MWCNTs-W.

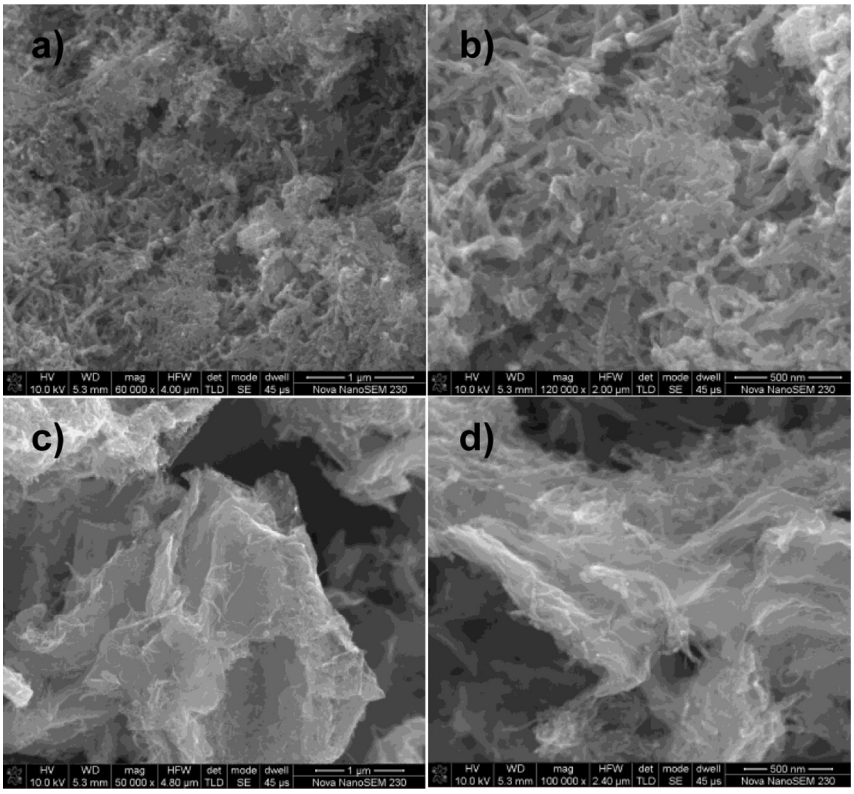

Fig. 3. SEM images of (a) and (b) the MWCNTs-W/S composite, (c) and (d) the RGO@MWCNTs-W/S composite.

its hydrophilicity [33], which would be helpful for the fine distribution of sulfur in the MWCNTs-W matrix.

SEM images of the as-prepared MWCNTs-W/S composite and the RGO@MWCNTs-W/S composite are presented in Fig. 3. It is clearly seen from Fig. 3 (a) and (b) that the MWCNTs were intertwined with one another, showing a webs structure. No large bulk sulfur particles can be easily observed, suggesting that the sulfur is uniformly embedded in the MWCNTs-W structure and form an inseparable complex. As shown in Fig. 3 (c) and (d), a flexible and corrugated thin-film can be clearly observed outside the MWCNTs-W/S composite, which indicates that the MWCNTs-W/S are completely enfolded by sheets of graphene with the use of SDS (a cationic surfactant). In order to verify the microstructure further, TEM images of the MWCNTs-W/S composite and the RGO@MWCNTs-W/S composite are shown in Fig. 4. Obviously, the MWCNTs-W/S composite was tightly covered by the graphene thin-film, forming a three-dimensional hybrid nanostructure. This unique structure will be benefit to

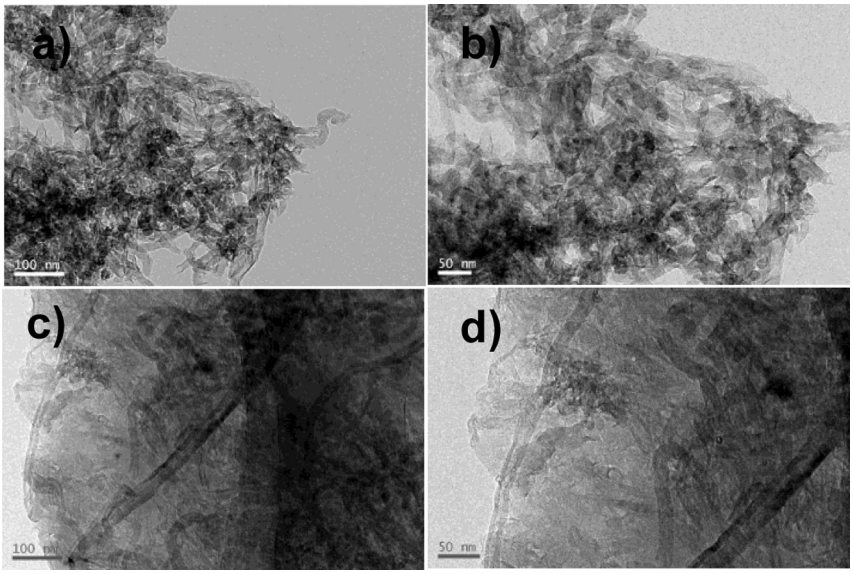

Fig. 4. TEM images of (a) and (b) the MWCNTs-W/S composite, (c) and (d) the RGO@MWCNTs-W/S composite.

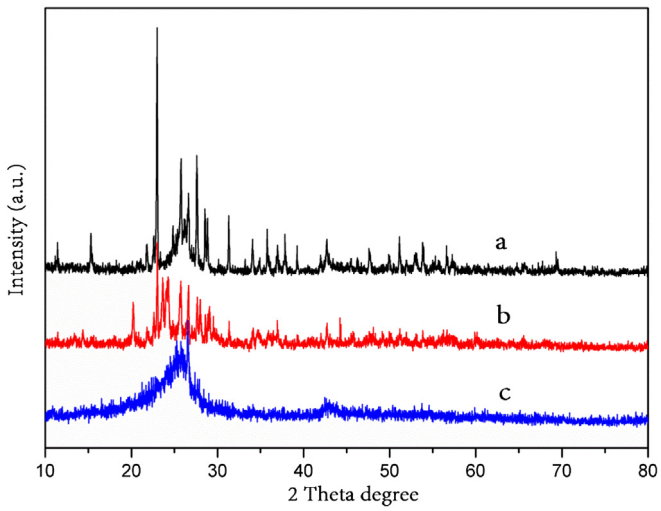

Fig. 5. the XRD patterns of (a) the simple mixture of MWCNTs-W/sulfur powder, (b) the MWCNTs-W/S composite and (c) the RGO@MWCNTs-W/S composite.

shorten the path for Li^+ ion and electronic transport, leading to a superior rate cycling performance.

The X-ray-diffraction (XRD) patterns of the simple mixture of MWCNTs-W/sulfur powder, the as-prepared MWCNTs-W/S composite and the RGO@MWCNTs-W/S composite are presented in Fig. 5. Similar to the pattern of the MWCNTs-W/sulfur power, the characteristic peaks of sulfur can be detected in the MWCNTs-W/S composite, suggesting that amount of sulfur was crystallized on the outer surface of the MWCNTs and the sulfur loading process for the MWCNTs-W/S composite did not bring any structure change for sulfur [19,31]. However, the diffraction intensity of peaks of sulfur in the MWCNTs-W/S composite were weaker than those of the simple mixture of MWCNTs-W/sulfur powder, which was probably due to the infiltration of sulfur into the channels and pores of the MWCNTs-W. Most importantly, no obvious characteristic sulfur peaks can be easily observed in the XRD pattern of the RGO@MWCNTs-W/S composite, and only a broad peak representing the carbon content around 26° appears, which indicates the MWCNTs-W/S composite was perfectly wrapped by the RGO [36,41]. Furthermore, the uniform distribution of sulfur in the composites were confirmed by EDS mapping analysis on the MWCNTs-W/S composite and the RGO@MWCNTs-W/S composite, respectively, as shown in Fig. 6 (a), (b), (c) and (d), (e), (f).

As shown in Fig. 7 (a), TGA was carried out to measure the accurate sulfur content in the MWCNTs-W/S composite and the RGO@MWCNTs-W/S composite. The TGA curves depict weight losses of the composite correlated to the sublimation of sulfur under N_2 atmosphere, and the sulfur content in the MWCNTs-W/S composite and the RGO@MWCNTs-W/S composite are 79.61 wt% and 68.93 wt%, respectively. Therefore, the content of RGO and MWCNTs-W in the RGO@MWCNTs-W/S composite are 13.41 wt% and 17.66 wt%, respectively. In addition, compared with the MWCNTs-W/S composite, the TGA curve of the RGO@MWCNTs-W/S composite was much more flat, which may be due to the retarding effect of the RGO when the subliming sulfur was escaping from the composite under high temperature, further indicating that the RGO@MWCNTs-W/S composite has a nice encapsulation capability [36,45].

In order to demonstrate the advantageous electrochemical properties of the RGO@MWCNTs-W/S composite, MWCNTs-W/S composite with 68.93 wt% sulfur was prepared by the same melt-diffusion strategy for comparison. Fig. 7 (b) shows the cyclic voltammograms of the RGO@MWCNTs-W/S composite in the voltage window of 3.0–1.6 V at a scan rate of 0.2 mv s^{-1}. Two separated cathodic peak potentials at 2.4–2.1 V and 2.1–1.8 V (versus Li/Li^+) can be easily observed, corresponding to the conversion of elemental sulfur to lithium polysulfides (Li_2S_x, $8 > x \geq 4$) and lithium polysulfides to solid-state Li_2S_2/Li_2S, respectively [22,27]. However, Two separated oxidation peaks potentials with somewhat overlapping features at the voltage range from 2.6 V to 2.3 V can be observed, suggesting a two-plateau oxidation process, i.e. the reversible oxidation reaction from solid Li_2S/Li_2S_2 to short-chain polysulfides (Li_2S_n, $n > 2$) and then to the element sulfur or the final oxidation of the polysulfides [17,29,47], which is different from the only one anodic peak potential at 2.4 V reported in other literature [19,20]. More importantly, after the second cycle, the CV profiles were relatively overlapping, implying an excellent electrochemical reversibility.

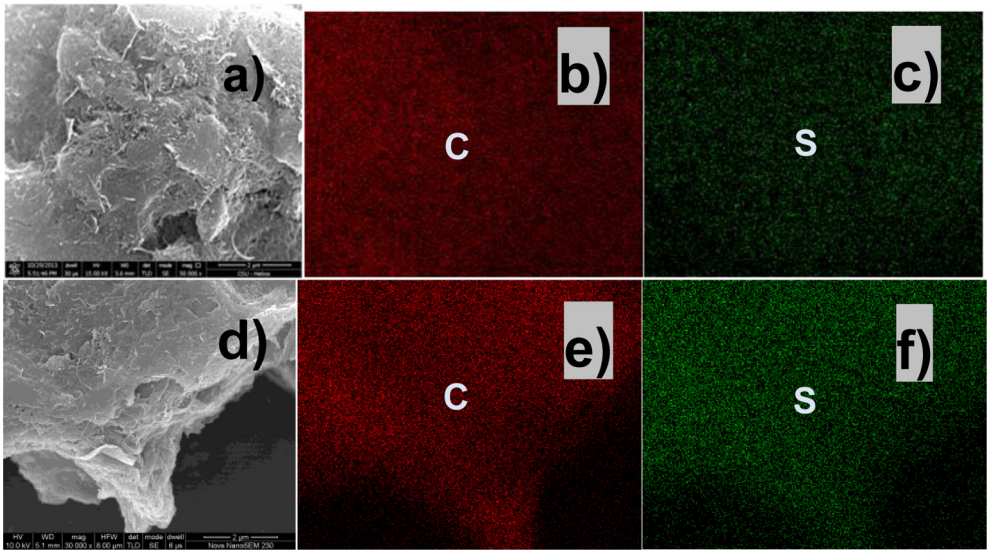

Fig. 6. (a) SEM image of the MWCNTs-W/S composite, (b) EDS carbon mapping for the region shown in (a), (c) EDS sulfur mapping for the region shown in (a), (d) SEM image of the RGO@MWCNTs-W/S composite, (e) EDS carbon mapping for the region shown in (d), (f) EDS sulfur mapping for the region shown in (d).

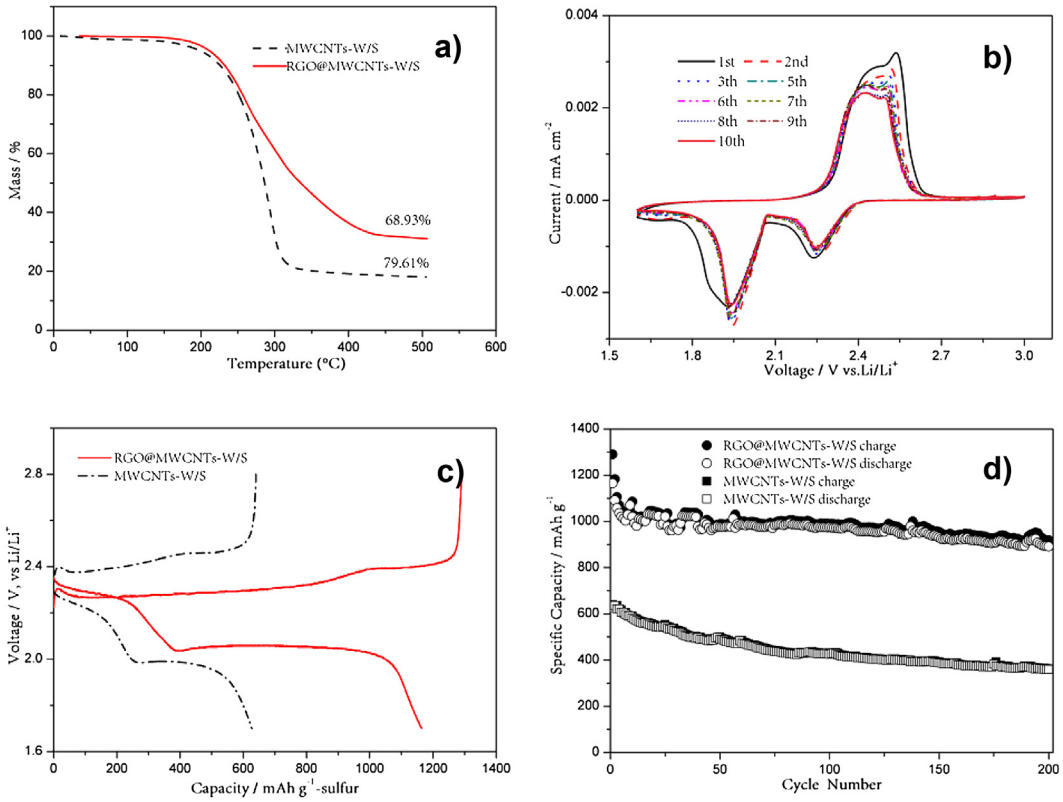

Fig. 7. TGA curves recorded for the MWCNTs-W/S composite and the RGO@MWCNTs-W/S composite under nitrogen flow (a), Cyclic voltammograms of the RGO@MWCNTs-W/S cathode in the potential window from 1.6 to 3.0 V (versus Li/Li$^+$) at the scan rate of 0.2 mV s^{-1}(b), the initial discharge/charge curves of the lithium-sulfur batteries with the MWCNTs-W/S composite cathode and the RGO@MWCNTs-W/S composite cathode at 1 C (c), cycling performances of the MWCNTs-W/S composite and the RGO@MWCNTs-W/S composite at 1 C (d).

The initial charge/discharge potential profiles at 1 C, and the cycling stabilities of the MWCNTs-W/S composite and the RGO@MWCNTs-W/S composite are shown in Fig. 7 (c) and (d), respectively. As shown in Fig. 7 (c), there are two discharge potential plateaus and two charge potential plateaus in both discharge/charge profiles. However, in the initial discharge curve of the RGO@MWCNTs-W/S composite, the two discharge potential plateaus, one at ~2.30 V and the other at ~2.05 V (vs Li/Li$^+$), are much higher than those of the MWCNTs-W/S composite, while the two charge potential plateaus in the initial charge curve of the RGO@MWCNTs-W/S composite, one at ~2.20 V and the other at ~2.30 V (vs Li/Li$^+$), are much lower than those of the MWCNTs-W/S composite respectively. This result indicates that the RGO@MWCNTs-W/S composite has a relatively low potential polarization and good reversibility [17]. What's more, the second discharge potential plateau of the RGO@MWCNTs-W/S composite was much wider, contributing to the majority of the discharge capacity, and a high initial specific capacity of up to 1164.5 mA h g^{-1} was obtained, corresponding to 69.3% of the theoretical capacity of sulfur. This means at least 1.39 electrons per sulfur atom were involved in the electrochemical reactions of the RGO@MWCNTs-W/S composite. On the contrary, the initial specific capacity of the MWCNTs-W/S composite is 628 mA h g^{-1}, about 37.4% of the theoretical capacity of sulfur, indicating that only 0.75 electrons per sulfur atom were involved in the electrochemical reactions of the MWCNTs-W/S composite. Meanwhile, as shown in Fig. 7 (d), after 200 cycles, a high discharge capacity of 891.5 mAh g^{-1} still remained for the RGO@MWCNTs-W/S composite at 1 C. However, a low discharge capacity of 359 mAh g^{-1} was retained for the MWCNTs-W/S composite at 1 C. It is noted that the electrochemical performance of the MWCNTs-W/S composite is some poorer than that of the same materials system reported by other researchers. [25,29], which should be due to the different sulfur loading in the composites. Thus, in consideration of the high sulfur content in the MWCNTs-W/S composite (68.91 wt%) and the normal method to prepare the cathode, the electrochemical performance of the MWCNTs-W/S composite in our article was reasonable and acceptable to some extent. Meanwhile, the superior high active-sulfur utilization and outstanding capacity retention evidences the efficient accessibility of active sulfur and the effective prevention of the shuttle reaction in the RGO@MWCNTs-W/S composite.

Moreover, because of the three-dimensional hybrid nanostructure acting as a 3D conductive network with excellent Li$^+$ ion transport, the RGO@MWCNTs-W/S composite displayed high specific capacities and excellent cycling stabilities even cycled at higher rates. As shown in Fig. 8 (a), after the initial activation processes at a low rate of 1 C, the RGO@MWCNTs-W/S composite cathodes were cycled at 2 C and 5 C, respectively. Although both of the discharge capacities faded gradually during the initial cycling at 1 C, the capacities then remained constant at 807 mAh g^{-1} for 2 C and 620 mAh g^{-1} for 5 C after 200 cycles, with an average coulombic efficiency of 97% and 96%, respectively. To further investigate the high rate performance of the RGO@MWCNTs-W/S composite, a rate capacity study was carried out at various rates (Fig. 8 (b)). Although, the discharge capacity gradually decreased at 1 C rate, when the current rate increased to 2 C, 3 C and 5 C, the RGO@MWCNTs-W/S composites delivered a capacity of 890.5 mAh g^{-1}, 845.4 mAh g^{-1} and 727.2 mAh g^{-1}, respectively. After cycling at various rates, when the current rate was turned back to 1 C, a stable capacity of 813.2 mAh g^{-1} was resumed even

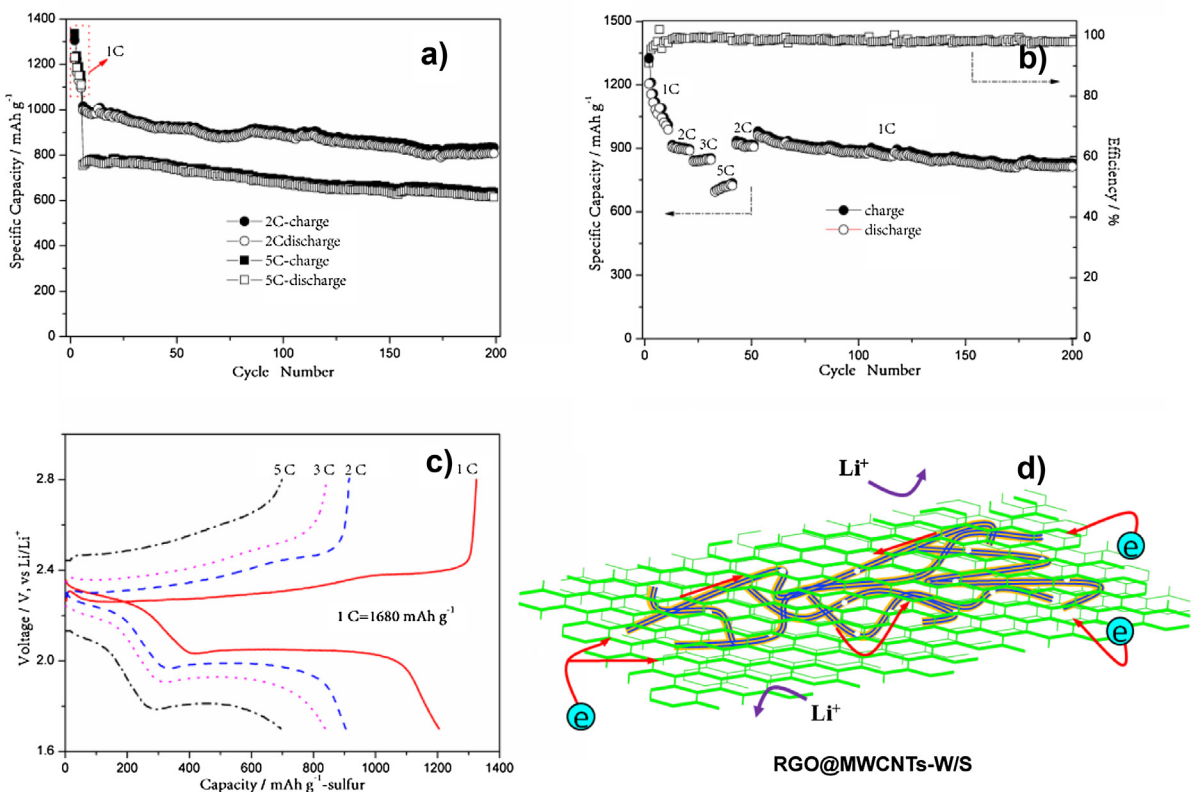

Fig. 8. Cycling performances of the RGO@MWCNTs-W/S composite at 2 C and 5 C (a), rate capability of the RGO@MWCNTs-W/S composite (b), the discharge/charge curves of the RGO@MWCNTs-W/S composite cathode for every 10th cycle at each rate (c), scheme of the RGO@MWCNTs-W/S composite for improving the cathode performance (d).

after 200 cycles. As shown in Fig. 8 (c), with the increase in the current rate from 1 C to 5 C, the typical two discharge voltage plateaus of sulfur cathode still maintained.

Such high capacity and stable cyclability for sulfur cathode at this high rate are unprecedented. The highly desirable electrochemical performance attributes to the unique three-dimensional hybrid nanostructure, as shown in Fig. 8 (d). First, after activation with KOH, not only parts of the closed ends of MWCNTs were opened, but also its surface became rough and porous, which will contribute to the incorporation of sulfur and the adsorption of polysulphides anions. Second, the as-modified MWCNTs self-weaved into a web-structure, and then were tightly covered by the graphene thin-film to form a three-dimensional hybrid nanostructure, which will shorten the path for Li^+ ion and electronic transport, leading to the superior rate cycling performance. What's more, due to the residual oxygen-containing functional groups on the surface of RGO, polysulphides anions can be further adsorbed in the cathode, minimizing the shuttle reaction and mass loss of the active materials during cycles [6,29–32,36]. Therefore, the RGO@MWCNTs-W/S composites showed a high rate capability and excellent cycling performance.

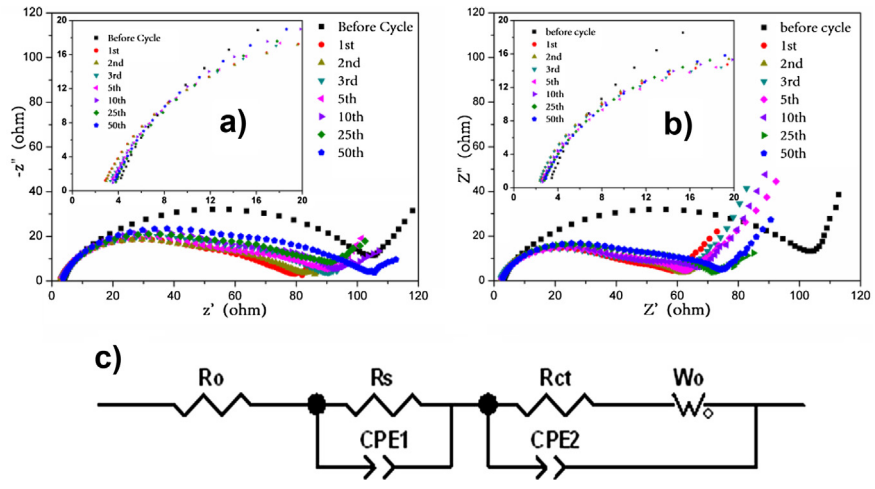

Fig. 9. EIS data for the lithium-sulfur half cells with the MWCNTs-W/S composite (a) and the RGO@MWCNTs-W/S composite (b) as cathodes between 0.01 and 10^5 Hz, the relevant equivalent circuit model (c).

To further investigate the electrochemical reaction process, electrochemical impedance spectra of the RGO@MWCNTs-W/S composite electrode and the MWCNTs-W/S composite electrode before cycling and at fully charged in different cycles at 1 C were measured. As shown in Fig. 9 (a) and (b), before cycling, the semicircle at high frequency associates with the charge transfer resistance (R_{ct}) of the sulfur electrode [10,48]. After cycling, all of the impedance spectra are composed of two semicircles in the middle-high frequency domain and an inclined line in the low frequence region. The semicircle at high frequency associates with the SEI film formed on the electrodes' surface (R_s), the other one at middle frequency associates with R_{ct}, and the straight line in the low frequence associates with the Warburg impedance (W_0). The intercept at real axis Z', corresponding to the combination resistance R_o, associates with the ionic resistance of the electrolyte, the intrinsic resistance of the active materials and the contact resistance at the active material/current collector interface [45,49–52].

In order to understand those phenomena better, a relevant equivalent circuit model was given (as shown in Fig. 9 (c)), and the related electrodes resistance data were obtained (as shown in Table 1). After the first cycle, it is clear that the resistance of the two electrodes drastically decrease, which is due to a chemical activation process of the dissolution and redistribution of the active material. R_o of the RGO@MWCNTs-W/S composite electrode almost holds constant with only a slight increase (2.20 Ω in the 1st cycle, 2.35 Ω in the 50th cycle), which is lower than that of the MWCNTs-W/S composite electrode (2.37 Ω in the 1st cycle, 3.41 Ω in the 50th cycle). It demonstrates that the conductivity of the RGO@MWCNTs-W/S composite is better. Meanwhile, R_s of the RGO@MWCNTs-W/S composite electrode after 1 cycle (37.59 Ω) and after 50 cycles (47.22 Ω) are much lower than those of the MWCNTs-W/S composite electrode (51.28 Ω in the 1st cycle, 64.78 Ω in the 50th cycle), respectively, which means a more stable SEI film formed on the surface of lithium, leading to the minimization of shuttling reaction and a stable cycle performance. Although R_{ct} of the two cathodes are almost the same after the chemical activation process, R_{ct} of the MWCNTs-W/S composite electrode significantly increases as cell cycles to the 50th (40.05 Ω), which results from the irreversible deposition and aggregation of insulated Li_2S_2/Li_2S on the MWCNTs-W surface. On the contrary, R_{ct} of the RGO@MWCNTs-W/S composite electrode only increases a little (23.32 Ω in the 1st cycle, 26.17 Ω in the 50th cycle), which means the RGO@MWCNTs-W/S composite favors the fast charge-transfer response [52]. W_o is the Warburg impedance due to the diffusion of the lithium-ion within the cathode [17,36,53], and the angle of the inclined line to the Z'' axis reflects the change of W_0. During the cycling, the angles of the inclined line of the RGO@MWCNTs-W/S composite electrode are all larger than those of the MWCNTs-W/S composite electrode at the same cycle, respectively. This may be due to the unique three-dimensional hybrid nanostructure in which both of the RGO and the MWCNTs could provide an excellent Li^+ ion diffusion pathway. The EIS results further explain why the RGO@MWCNTs-W/S composite displays an admirable high-rate capability and cycling stability.

Table 1
Electrode resistance obtained from the equivalent circuit fitting of experimental data.

Cycle	MWCNTs-W/S			RGO@MWCNTs-W/S		
	R_o (Ω)	R_s (Ω)	R_{ct} (Ω)	R_o (Ω)	R_s (Ω)	R_{ct} (Ω)
0	3.71	–	107.21	3.44	–	104.71
1	2.37	51.28	23.35	2.20	37.59	23.32
2	2.42	52.75	30.22	2.23	38.32	24.25
3	2.78	56.15	32.56	2.24	38.69	24.52
5	2.94	57.23	32.75	2.27	39.66	24.68
10	3.09	58.86	35.13	2.30	40.72	24.93
25	3.35	59.12	36.32	2.32	44.28	25.15
50	3.41	64.78	40.05	2.35	47.22	26.17

4. Conclusion

A three-dimensional hybrid nanostructure with the excellent Li^+ ion and electronic transport properties has been designed in this work. Not only can the unique nanostructure highly ensure a good electrical path for the active sulfur, but also can effectively trap soluble polysulfide intermediates. As compared with the MWCNTs-W/S composite, an exceptional high-rate charge/discharge capability was obtained for the RGO@MWCNTs-W/S composite with 68.91 wt% sulfur. In particular, even at an ultra-high rate (5 C), a discharge capacity as high as 620 mAh g^{-1} was retained for the RGO@MWCNTs-W/S composite after 200 cycles, with an average coulombic efficiency of 96%. We believed that the strategy of developing a hybrid structure by incorporating the merits of the MWCNTs webs and the reduced graphene oxide makes much sense to the structure designing of novel sulfur-based materials and the RGO@MWCNTs-W/S composite is a very promising cathode material for high-rate performance lithium-sulfur batteries.

Acknowledgments

This study was supported by the National Nature Science Foundation of China (51274240 and 51204209).

References

[1] X. Ji, L.F. Nazar, J. Mater. Chem. 20 (2010) 9821–9826.
[2] X. Ji, K.T. Lee, L.F. Nazar, Nat. Mater. 8 (2009) 500.
[3] C. Zu, A. Manthiram, Adv. Energy Mater. 3 (2013) 1008–1012.
[4] S. Lu, Y. Cheng, X. Wu, J. Liu, Nano Lett. 13 (2013) 2485–2489.
[5] J. Nelson, S. Misra, Y. Yang, A. Jackson, Y. Liu, H. Wang, H. Dai, J.C. Andrews, Y. Cui, M.F. Toney, J. Am. Chem. Soc. 134 (2012) 6337–6343.
[6] L. Yin, J. Wang, F. Lin, J. Yang, Y. Nuli, Energy Environ. Sci. 5 (2012) 6966–6972.
[7] G.Y. Zheng, Y. Yang, J.J. Cha, S.S. Hong, Y. Cui, Nano Lett. 11 (2011) 4462–4467.
[8] J.H. Shin, E.J. Cairns, J. Power Sources 177 (2008) 537–545.
[9] M. Nagao, A. Hayashi, M. Tatsumisago, Electrochem. Acta 56 (2011) 6055–6059.
[10] S. Zhang, Electrochem. Acta 70 (2012) 344–348.
[11] R. Xu, I. Belharouak, J.C.M. Li, X. Zhang, I. Bloom, J. Bareño, Adv. Energy Mater. 3 (2013) 833–838.
[12] L. Suo, Y. Hu, H. Li, M. Armand, L. Chen, Nat. Commun. 4 (2013) 1481.
[13] C. Barchasz, J. Leprêtre, F. Alloin, S. Patoux, J. Power Sources 199 (2012) 322–330.
[14] S. Xiong, K. Xie, Y. Diao, X. Hong, Electrochem. Acta 83 (2012) 78–86.
[15] Y.Z. Fu, A. Manthiram, RSC Adv. 2 (2012) 5927–5929.
[16] F. Wu, J.Z. Chen, R.J. Chen, S.X. Wu, L. Li, S. Chen, T. Zhao, J. Phys. Chem. C 115 (2011) 6057–6063.
[17] G.C. Li, G.R. Li, S.H. Ye, X.P. Gao, Adv. Energy Mater. 2 (2012) 1238–1245.
[18] L. Xiao, Y. Cao, J. Xiao, B. Schwenzer, M. Engelhard, L.V. Saraf, Z. Nie, G.J. Exarhos, J. Liu, J. Mater. Chem. A 1 (2013) 9517–9526.
[19] X. Liang, Z.Y. Wen, Y. Liu, H. Zhang, L.Z. Huang, J. Jin, J. Power Sources 196 (2011) 3655–3658.
[20] S.R. Chen, Y.P. Zhai, G.L. Xu, Y.X. Jiang, D.Y. Zhao, J.T. Li, L. Huang, S.G. Sun, Electrochem. Acta 56 (2011) 9549–9555.
[21] G. He, X.L. Ji, L. Nazar, Energy Environ. Sci. 4 (2011) 2878–2883.
[22] D.W. Wang, G.M. Zhou, F. Li, K.H. Wu, G.Q. Lu, H.M. Cheng, L.R. Gentle, Phys. Chem. Chem. Phys. 14 (2012) 8703–8710.
[23] J. Wang, S.Y. Chew, Z.W. Zhao, S. Ashraf, D. Wexler, J. Chen, S.H. Ng, S.L. Chou, H.K. Liu, Carbon 46 (2008) 229–235.
[24] F. Sun, J. Wang, H. Chen, W. Li, W. Qiao, D. Long, L. Ling, ACS Appl. Mater. Interfaces 5 (2013) 5630–5638.
[25] J.J. Chen, Q. Zhang, Y.N. Shi, L.L. Qin, Y. Cao, M.S. Zheng, Q.F. Dong, Phys. Chem. Chem. Phys. 14 (2012) 5376–5382.
[26] L.X. Yuan, H.P. Yuan, X.P. Qiu, L.Q. Chen, W.T. Zhu, J. Power Sources 189 (2009) 1141–1146.
[27] J.C. Guo, Y.H. Xu, C.H. Wang, Nano Lett. 11 (2011) 4288–4294.
[28] W. Wei, J.L. Wang, L.J. Zhou, J. Yang, B. Schumann, Y. NuLi, Electrochem. Commun. 13 (2011) 399–402.
[29] Y. Su, Y. Fu, A. Manthiram, Phys. Chem. Chem. Phys. 14 (2012) 14495–14499.

[30] L. Ji, M. Rao, S. Aloni, L. Wang, E.J. Cairns, Y. Zhang, Energy Environ. Sci. 4 (2011) 5053–5059.
[31] S. Zhang, Q. Zhang, J. Huang, X. Liu, W. Zhu, M. Zhao, W. Qian, F. Wei, Part. Part. Syst. Charact. 30 (2013) 321–325.
[32] X. Zhang, Q. Sun, W. Dong, D. Li, A. Lu, J. Mu, W. Li, J. Mater. Chem. A 1 (2013) 9449–9455.
[33] C. He, S. Song, J. Liu, V. Maragou, P. Tsiakaras, J. Power Sources 195 (2010) 7409–7414.
[34] M. He, L. Yuan, W. Zhang, Y. Huang, J. Solid State Electr. 17 (2013) 1641–1647.
[35] Z.Q. Tian, S.P. Jiang, Y.M. Liang, P.K. Shen, J. Phys. Chem. B 110 (2006) 5343–5350.
[36] X. Zhou, J. Xie, J. Yang, Y. Zou, J. Tang, S. Wang, L. Ma, Q. Liao, J. Power Sources 243 (2013) 993–1000.
[37] H. Wang, Y. Yang, Y. Liang, J.T. Robinson, Y. Li, A. Jackson, Y. Cui, H. Dai, Nano Lett. 11 (2011) 2644–2647.
[38] M. Zhao, X. Liu, Q. Zhang, G. Tian, J. Huang, W. Zhu, F. Wei, ACS Nano 6 (2012) 10759–10769.
[39] F. Wu, J. Chen, L. Li, T. Zhao, Z. Liu, R. Chen, ChemSusChem 6 (2013) 1438–1444.
[40] M. Xiao, M. Huang, S. Zeng, D. Han, S. Wang, L. Sun, Y. Meng, RSC Adv. 3 (2013) 4914–4916.
[41] N. Li, M. Zheng, H. Lu, Z. Hu, C. Shen, X. Chang, G. Ji, J. Cao, Y. Shi, Chem. Commun. 48 (2012) 4106–4108.
[42] L.W. Ji, M.M. Rao, H.M. Zheng, L. Zhang, Yu.C. Li, W.H. Duan, J.H. Guo, E.J. Cairns, Y.G. Zhang, J. Am. Chem. Soc. 133 (2011) 18522–18525.
[43] S. Evers, L.F. Nazar, Chem. Commun. 48 (2012) 1233–1235.
[44] B. Ding, C. Yuan, L. Shen, G. Xu, P. Nie, Q. Lai, X.G. Zhang, J. Mater. Chem. A 1 (2013) 1096–1101.
[45] X. He, L. Wang, J. Li, J. Gao, M. Fang, G. Tian, J. Wang, S. Fan, J. Power Sources 239 (2013) 623–627.
[46] S. Stankovich, R. Piner, S. Nguyen, R. Ruoff, Carbon 44 (2006) 3342–3347.
[47] S. Chung, A. Manthiram, J. Mater. Chem. A 1 (2013) 9590–9596.
[48] L. Yuan, X. Qiu, L. Chen, W. Zhu, J. Power Sources 189 (2009) 127–132.
[49] M. Rao, X.Y. Song, E.J. Cairns, J. Power Sources 205 (2012) 474–478.
[50] Y. Wang, L. Huang, L. Sun, S. Xie, G. Xu, S. Chen, Y. Xu, J. Li, S. Chou, S. Dou, S. Sun, J. Mater. Chem. 22 (2012) 4744–4750.
[51] J. Kim, D. Lee, H. Jung, Y. Sun, J. Hassoun, B. Scrosati, Adv. Funct. Mater. 23 (2013) 1076–1080.
[52] L.L. Zhang, S.Y. Zhao, X.N. Tian, X.S. Zhao, Langmuir 26 (2010) 17624–17628.
[53] Y. Fu, Y. Su, A. Manthiram, ACS Appl. Mater. Interfaces 4 (2012) 6046–6052.